LensFD: Using Lenses for Improved Sub-6 GHz Massive MIMO Full-Duplex

Zhican Chen , *Student Member, IEEE*, C. Nicolas Barati , *Member, IEEE*, Jon Veihl , *Member, IEEE*, Clayton Shepard, *Member, IEEE*, and Ashutosh Sabharwal , *Fellow, IEEE*

Abstract-Massive MIMO has emerged as a key-enabler to deliver the high data-rates in current and next-generation systems. Many massive MIMO deployments use time-division duplex (TDD), thereby opening the door for the potential use of full-duplex at base-stations. In this paper, we present LensFD, a scalable method to enable cost-effective massive MIMO full-duplex operation in sub-6 GHz frequencies with a focus on the CBRS band of 3.5 GHz. LensFD uses a low-cost lens array combined with transmit precoding to reshape the effective beam pattern of antennas in massive MIMO arrays to reduce self-interference. We tested three lens configurations in LensFD experimentally with a software-defined 40-antenna base-station and demonstrate a significant improvement in self-interference reduction and hence overall increased system capacity to $1.6 \times$ over the TDD counterpart. As an important contribution, we will open-source the large measurement dataset from our experiments.

Index Terms—Massive MIMO, full-duplex, dielectric spherical lenses, precoding, experimental design.

I. INTRODUCTION

ASSIVE MIMO is one of the major technology drivers of next-generation wireless standards (5G and beyond) [1], [2]. By using base-stations with hundreds of antennas [3], [4], [5], the networks can achieve both increased capacity [6] and improved energy efficiency [7], [8]. One of the key challenges due to a large number of antennas is that channel measurement in frequency-division duplex (FDD) mode becomes prohibitive [9]; FDD is the dominant duplexing mode in LTE and prior standards [10], [11]. As a result, many 5G deployments use time-division duplex (TDD). This shift from FDD to TDD opens up the door to the use of in-band full-duplex (IBFD) [12], [13], [14], [15], [16] in the upcoming iterations of 5G and beyond [17], [18].

Full-duplex is a wireless communication paradigm that allows concurrent transmission and reception on the same time-frequency resources [12], [13], [14], [15], [16], [19]. It has

Manuscript received 1 June 2022; revised 17 November 2022; accepted 7 January 2023. Date of publication 30 January 2023; date of current version 20 June 2023. This work was supported in part by NSF under Grants CNS-2120363 and CNS-2106993, and in part by NSF PAWR under Grant CNS-1827940. The review of this article was coordinated by Dr. Nghi H. Tran. (Corresponding author: Zhican Chen.)

Zhican Chen, C. Nicolas Barati, and Ashutosh Sabharwal are with the Department of Electrical and Computer Engineering, Rice University, Houston 77005 USA (e-mail: zc38@rice.edu; nicobarati@rice.edu; ashu@rice.edu).

Jon Veihl is with the CommScope, Lisle, IL 60532 USA (e-mail: jon.veihl@commscope.com).

Clayton Shepard is with the Skylark Wireless, Houston 77006 USA (e-mail: clay@skylarkwireless.com).

Digital Object Identifier 10.1109/TVT.2023.3240558

the potential of doubling the capacity [16], [20], [21] compared to half-duplex, e.g., TDD or FDD. Realization of a full-duplex system hinges on combating self-interference, which is the interference created by simultaneous transmission and reception. Complete cancellation or at least significant reduction of self-interference has thus been the main focus of research in full-duplex, resulting in a large body of work on this topic.

For massive MIMO base-stations, there are (at least) two classes of full-duplex architectures. The first class relies on analog-cancellation-based reduction of self-interference, where self-interference suppression/cancellation is performed before the signal passes through an analog-to-digital converter. The work on analog cancellation started with single-antenna [22], [23] and dual-antenna [14], [15], [16] systems. However, these analog-cancellation-based designs of massive MIMO with 64-256 antennas [17] have high analog circuit complexity, typically $O(N^2)$ analog circuit complexity for a $N \times N$ antenna array. Recent works [24], [25] have reduced the complexity to O(NK) where K is the number of transmit beams.

The second class of massive MIMO full-duplex systems uses transmit precoding to reduce self-interference. The precoding-based methods dynamically partition the antenna array composed of only half-duplex transceivers into two sub-arrays, one which transmits and the other which receives. Transmit beamforming is performed to focus energy toward intended downlink users while also suppressing self-interference to the receive sub-array [12], [13], [26], [27]. These solutions have to tradeoff self-interference suppression with downlink transmission degrees-of-freedom (DoF) and can be desirable for a large number of antennas.

From the operator point-of-view, having access to two classes of massive MIMO full-duplex architectures is desirable as they occupy different performance-cost points. The first class achieves higher full-duplex performance but requires more design complexity (e.g., design of new circuits) and hence system cost. The second class achieves a lower performance as it sacrifices some downlink transmission degrees-of-freedom for self-interference suppression but is also lower in costs. In fact, the second class of solutions can be used with any half-duplex radios and can in fact, be layered on top of existing TDD base-stations.

In this paper, we push the performance of the second class of systems with the use of low-cost spherical dielectric lenses that can be added to the base-stations. Our proposed design is simple and can significantly improve the performance of precodingbased full-duplex massive MIMO in outdoor deployment cases. Our contributions are three-fold.

First, we propose a first-of-its-kind study of using lenses for self-interference suppression to enable scalable sub-6 GHz full-duplex operations. Most of the prior work in the use of lenses focused on mmWave systems [28], [29], [30], [31], [32], [33], [34] and have typically adopted a single lens with size either comparable to or much larger than the antenna array. The mmWave lenses are typically elliptical or hemispherical shaped and require delicate installation such that the antennas are placed near the focal point. For sub-6 GHz, metasurface lenses [35], [36] have been used to reduce beamforming complexity and power consumption in massive MIMO systems. In [37], a lens-loaded spiral aperture with 8 antennas operating at sub-6 GHz is proposed for in-band full-duplex applications, where lenses are used to enhance the system's far-field performance instead of suppressing self-interference. To the best of our knowledge, LensFD is the first sub-6 GHz proposal to reduce self-interference for massive MIMO full-duplex systems by using passive lenses.

Second, we perform an extensive experimental evaluation. Our evaluation is performed both at antenna-scale in an anechoic chamber, and for the full array using a deployed commercialgrade 40-antenna massive MIMO base-station. Our main result shows that a lens-array alone can suppress self-coupling strength by up to 7 dB in a typical outdoor environment. This gain is obtained without any change to the underlying TDD base-station. When combined with a digital precoder, LensFD consistently yields more self-interference suppression over the no lens baseline across different transceiver configurations and downlink receive power setups. LensFD can also push the self-interference to close to the noise floor for certain transmit-receive antenna partitions. The additional self-interference suppression from LensFD translates into achievable rate gain in both uplink and downlink, yielding up to 1.6× sum-rate gain over the systems with no lens.

An important outcome of our experimental evaluations is that the antenna-scale characterization is not sufficient to predict deployed system-scale full-duplex performance. The main reason is that self-interference depends on both direct and backscatter paths between transmit and receive antennas. This fact explains one of our results - even if lenses improve antenna gain and reduce half-power beamwidth, they lead to a negligible full-duplex gain in indoor systems, where the backscatter has a significant contribution to self-interference. In contrast, when the backscatter is low, like in outdoor deployments, full-duplex gain from lenses is significant. However, here too, the per-antenna measurements do not predict which size lens-array will perform the best as self-interference in a UPA depends on interference from multiple antennas and lens shape self-interference from different transmit antennas in a complex manner.

Third, we will open-source our whole dataset and analysis scripts. The 101 GB dataset will provide a unique dataset from a commercial-grade system in realistic deployment scenarios.

The rest of the paper is organized as follows. In Section II, we describe the system model and the problem formulation.

In Section III, we provide measurement-based effective beam pattern analysis of LensFD. In Section IV, we present real-world channel trace measurements of LensFD resultant massive MIMO full-duplex channels. In Section V, we quantify the gains in overall self-interference suppression from LensFD. In Section VI, we summarize our findings.

Notation: We use bold uppercase and lowercase letters to denote matrices and column vectors, respectively; \dagger (as superscript) for Moore-Penrose pseudo-inverse; $\|\cdot\|_F$ for the Frobenius norm; $\|\cdot\|_2$ for the ℓ_2 -norm; S_1-S_2 for set subtraction; I for the identity matrix; $\mathbf{H}(S_r,S_c)$ represents the submatrix of matrix \mathbf{H} constructed from the rows and columns indexed by the sets S_r and S_c , respectively.

II. SYSTEM MODEL AND PROBLEM STATEMENT

A. Antenna Array Design

In this section, we describe the massive MIMO base-station configuration with only half-duplex radios. We will assume a Uniform Planar Array (UPA) structured base-station with $M_{\rm row}$ rows and $M_{\rm col}$ columns, for a total of $M=M_{\rm row}M_{\rm col}$ antennas. The base-station is assumed to communicate with K_u uplink and K_d downlink users simultaneously, where both uplink and downlink transmissions are in the same frequency band. Each mobile user has a half-duplex transceiver, i.e., they can either transmit or receive in the frequency band of operation but not do both simultaneously.

The in-band full-duplex operation is achieved by operating M_t out of M antennas in transmit mode, and the other $M_r = M - M_t$ antennas in receive mode. We denote the set of all transmit antennas as $S_t = \{s_i : i = 1, 2, \dots, M_t, 1 \leq s_i \leq M\}, |S_t| = M_t$ and of all receive antennas as $S_r = S_{bs} - S_t, |S_r| = M_r$, where each such (S_t, S_r) partition is referred to as a transceiver configuration. Any arbitrary transceiver configuration is easily achieved by placing the antennas in transmit or receive mode.

B. Lens Array Design

LensFD equips the massive MIMO base-station with an overlaid Radio-Frequency (RF) lens array [38], [39]. Each lens in the array is a passive transmissive device that can either focus or disperse the propagating electromagnetic wave. Assuming that there is only negligible propagation loss through each lens in the array, the total amount of radiation power remains constant with or without the lens array. To investigate the relationship between the lens array design and the resulting full-duplex performance, we designed and fabricated three lens arrays as shown in Fig. 1. As depicted in Fig. 1(b)–(d), each lens may cover one or more antennas depending on its size. In the case where a single lens covers multiple antennas, different antennas generally have different effective beam patterns since they are covered by different portions of the lens.

C. Signal Model

Let $\mathbf{H}_D \in \mathbb{C}^{K_d \times M}$, $\mathbf{H}_U \in \mathbb{C}^{M \times K_u}$, $\mathbf{H}_S \in \mathbb{C}^{M \times M}$ be the downlink, uplink and self-interference channels, respectively,

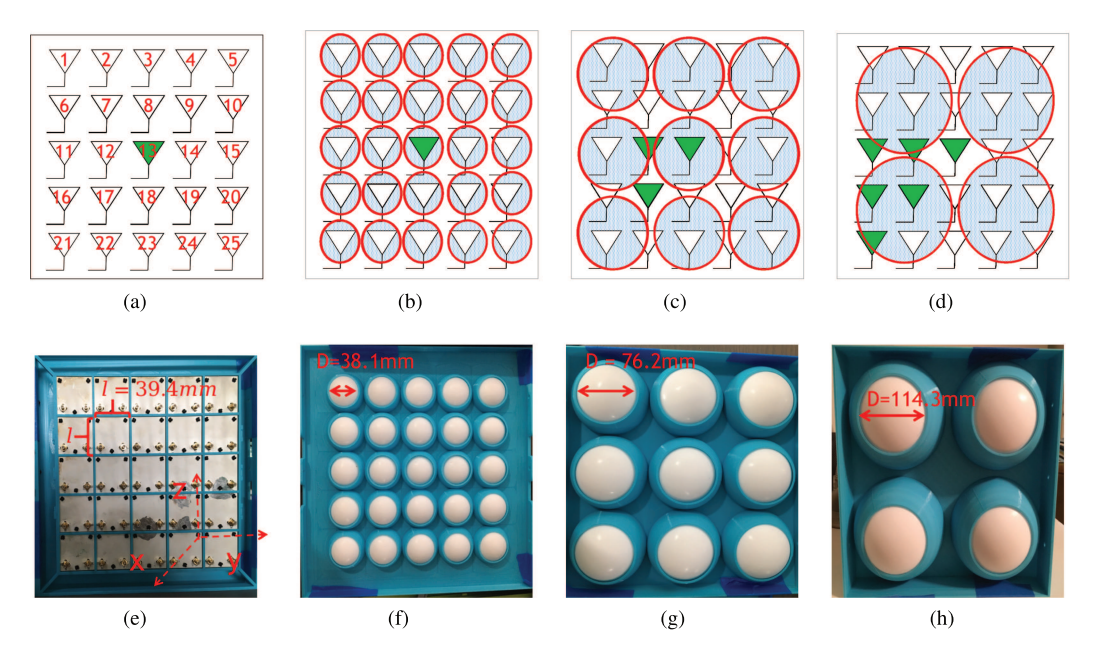


Fig. 1. LensFD massive MIMO base-station setup. (a)–(d): schematic diagram of the 5×5 antenna array and 3 different overlaid lens arrays with varying sizes. Lenses are shown as red circles, and antennas from the measurement sets $S_{\rm ms}$ are shown as green triangles. Indexing over the antenna array is shown in (a). (e)–(h): pictures of the antenna array and the lens arrays. (e) shows the rear view and (f)–(h) show the front view. (a) Antenna array indexing with *no lens*. (b) Antenna array with *small lens array*. (c) Antenna array with *medium lens array*. (d) Antenna array with *large lens array*. (e) 5×5 antenna array. (f) 5×5 *small lens array*. (g) 3×3 *medium lens array*. (h) 2×2 *large lens array*.

where all channels are assumed to be block fading. For a given transceiver configuration specified as S_t , the uplink, downlink, and self-interference channels are defined as follows,

$$\mathbf{H}_{u} = \mathbf{H}_{U}(S_{r},:) \in \mathbb{C}^{M_{r} \times K_{u}},$$

$$\mathbf{H}_{d} = \mathbf{H}_{D}(:,S_{t}) \in \mathbb{C}^{K_{d} \times M_{t}},$$

$$\mathbf{H}_{s} = \mathbf{H}_{S}(S_{r},S_{t}) \in \mathbb{C}^{M_{r} \times M_{t}},$$
(1)

With the uplink, downlink, and self-interference channels defined in Equation (1), the signal model is given by

$$egin{aligned} egin{aligned} oldsymbol{y}_d &= \mathbf{H}_d \mathbf{P} oldsymbol{x}_d + oldsymbol{w}_d \ oldsymbol{y}_u &= \mathbf{H}_u oldsymbol{x}_u + \mathbf{H}_s \mathbf{P} oldsymbol{x}_d + oldsymbol{w}_u \end{aligned} \end{aligned}$$

We assume that $x_d \in \mathbb{C}^{K_d \times 1}$, the downlink signal transmitted by the base-station, is precoded by a precoder $\mathbf{P} \in \mathbb{C}^{M_t \times K_d}$, where M_t is the cardinality of the chosen configuration S_t . The symbol $x_u \in \mathbb{C}^{K_u \times 1}$ denotes the uplink signal transmitted by all the K_u uplink users. Additionally, $\boldsymbol{y}_u \in \mathbb{C}^{M_r \times 1}$ and $\boldsymbol{y}_d \in \mathbb{C}^{K_d \times 1}$ denote the uplink and downlink received signals, respectively. Finally, $\mathbf{w}_u \sim \mathcal{CN}(0, \sigma_u^2 \mathbf{I}_{M_r})$ is the uplink receive noise, and $\boldsymbol{w}_d \sim \mathcal{CN}(0, \sigma_d^2 \mathbf{I}_{K_d})$ is the Gaussian approximation of the sum of downlink receive noise and Inter-User-Interference (IUI). The precoder **P** is designed to meet the downlink transmission requirements and suppress self-interference from the transmit antennas to the receive antennas at the base-station. The transmission power is constrained to not exceed unit power, i.e., $\|\mathbf{P}\boldsymbol{x}_d\|_F^2 \leq 1$ and $\|\boldsymbol{x}_u\|_F^2 \leq 1$. We also assume $\mathbb{E}[\|\boldsymbol{x}_d\|_F^2] =$ K_d and hence $\|\mathbf{P}\|_F^2 \leq 1$. Based on previous measurement results [13], we assume that all matrices mentioned above are full-rank.

Note that IUI is the interference at the downlink user's end due to the transmission of uplink users. A rich literature can be found regarding minimizing IUI by designing schedules [40], [41], [42], [43] and MAC layer protocols [44], [45]. We hereby assume that most of the IUI can be effectively eliminated using prior methods and the magnitude of residual IUI is close to that of downlink receiver noise power, and hence we do not explicitly model it.

D. Performance Metrics

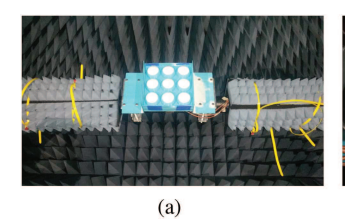
We will characterize two metrics for LensFD performance evaluation in massive MIMO full-duplex.

- 1) Residual Self-Interference: The residual self-interference is defined as the interference on the uplink signal from the concurrent downlink transmission signal (precoded by \mathbf{P}), i.e., $p_{si} = \|\mathbf{H}_s\mathbf{P}\|_F^2$. Since the goal of LensFD is to reduce the transmitted power in the self-interference channel \mathbf{H}_s , a lower value of the residual self-interference p_{si} indicates better full-duplex performance from LensFD.
- 2) Sum-Rate: The sum-rate α in massive MIMO full-duplex operations is defined as the summation of the uplink rate α_u and downlink rate α_d as $\alpha = \alpha_u + \alpha_d$, where

$$\alpha_u = K_u \log_2 \left(1 + \frac{p_{ul}}{(\sigma_u^2 + 10^{-\beta_{dc}/10} p_{si})} \right),$$

$$\alpha_d = K_d \log_2 \left(1 + \frac{p_{dl}}{\sigma_d^2} \right),$$
(3)

 $p_{ul} = \|\mathbf{H}_u\|_F^2/K_u$ and $p_{dl} = \|\mathbf{H}_d\mathbf{P}\|_F^2/K_d$ are the uplink and downlink receive power, respectively. We assume that the residual self-interference power can be cancelled by β_{dc} dB in the



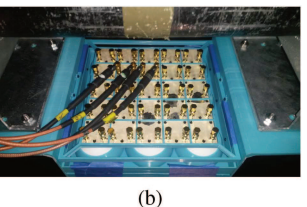


Fig. 2. Front and rear view of reflection-free anechoic chamber measurement setup for the 3×3 medium lens array placed in front of a 5×5 antenna array. (a) Front. (b) Rear.

digital domain by the M_r receiving antennas. Thus, the self-interference power after this digital cancellation is $10^{-\beta_{dc}/10}p_{si}$ as shown in Equation (3).

In addition to suppressing the self-interference power, LensFD also aims at strengthening the uplink and downlink receive power p_{ul} and p_{dl} . Combining all the power tuning effects, LensFD aims to achieve a higher sum-rate α as expressed in Equation (3).

III. PER-ANTENNA BEAM PATTERN CHARACTERIZATION

In this section, we present a measurement-based characterization of individual antenna patterns reshaped by differently-sized lenses. More specifically, we conducted 3D effective beam pattern measurements using three different lens configurations and compare them with the baseline case without a lens. For each configuration, we analyzed the corresponding main beam characteristics for antenna gain and half-power beamwidth. For the remainder of this section, we first introduce the experimental setup of the measurement and then describe the main results.

A. Experiment Design

We employed an automated indoor spherical near-field system developed by NSI [46] in the reflection-free environment of an anechoic chamber (see Fig. 2). As depicted in Fig. 1(e), the base-station consists of 25 patch antennas placed as a 5×5 rectangular UPA. The array lattice is square-shaped with a side length of 39.4 mm, approximately half the wavelength at the 3.5 GHz CBRS band. The antennas are dual slant linearly polarized supporting $\pm 45^{\circ}$ polarization.

All the lenses are spherically shaped and fabricated with dielectric PTFE Teflon material (dielectric constant $\epsilon_r=2.10$). The lens design in LensFD is inspired by the spherically symmetric gradient-index Luneberg lens [47], [48]. The key difference is that the fabricated lenses in LensFD employ a uniform dielectric material rather than a gradient. Such design not only simplifies the tradeoff analysis between the lens size and the resultant system performance, but also lowers the design complexity and fabrication cost, thus facilitating the real-world deployment of LensFD.

Three different lens configurations were fabricated and investigated in this paper, namely, *small lens array*, *medium lens array*, and *large lens array*. Throughout the rest of this paper, we compare the performance of these three configurations with the baseline configuration in which no lens is used, i.e., the *no lens*

TABLE I
LENS CONFIGURATION SETUPS AND CORRESPONDING MEASUREMENT SETS

Lens configuration	Single lens diameter (mm)	Cardinality	Measurement set S_{ms}
no lens	-	-	{13}
small lens array	38.1	5×5	{13}
medium lens array	76.2	3×3	{12, 13, 17}
large lens array	114.3	2×2	$\{11, 12, 13, 16, 17, 21\}$

configuration. As shown in Fig. 1, the diameter of each single lens is increased from 38.1 mm (i.e., same as the half-wavelength spacing distance for the 3.5 GHz CBRS band) for small lens array, to 76.2 mm for medium lens array and 114.3 mm for large lens array. For each lens configuration except for no lens, we embedded multiple identical lenses into a bracket to form the lens array. The brackets were made from polylactic acid (PLA) material with a dielectric constant $\epsilon_r = 1.46$, and were mounted in front of the base-station antenna array via bolts and rivets with a negligible distance in-between. The sizes of the three lens arrays are roughly the same, as more lenses are used for arrays with a smaller single lens diameter. For instance, we used $5 \times 5 = 25$ small lenses in *small lens array*. While in comparison, only $2 \times 2 = 4$ large lenses were used in *large lens* array. A more detailed description of each lens configuration can be found in Table I. In addition, the size of each lens array is also roughly the same as the size of the 5×5 base-station antenna array. As shown in Fig. 2, such an arrangement ensures that the antenna array is fully covered by the three lens arrays.

For each lens configuration, we performed 3D co-polarization effective beam pattern measurements in the far-field over a distinctive subset of all the base-station antennas, which is referred to as its measurement set $S_{\mathrm{ms}} \subset S_{\mathrm{bs}}$. As shown in Table I, S_{ms} includes all antennas covered by distinctive portions of the lens array in this configuration such that their effective beam patterns are representative of the entire antenna array. Note that we assume perfect hardware at the base-station so that the effective beam pattern of each antenna depends solely on the lens array covering it. That is, if two antennas i and j from two different positions in the array are covered by the same lens (or the same portion of the lens), they would have identical effective beam patterns as $f_i = f_i$. For example, when *small lens array* is used, each antenna is fully covered by a single lens. Therefore, one measurement over any arbitrary antenna is sufficient since all antennas share an identical effective beam pattern. Configurations with larger-sized lenses generally require more antennas to be measured since each single lens covers more antennas, and each such antenna generally yields different effective beam patterns. More details of each lens configuration and the corresponding measurement set $S_{\rm ms}$ can be found in Table I.

For each lens configuration, we activated each antenna port from its $S_{\rm ms}$ sequentially to measure its effective beam pattern. During each measurement, only one antenna port was excited while the rest were terminated with 50 Ω load resistance, which

¹For medium lens array, we have partial measurements due to COVID-19-related shutdowns

²We acknowledge that this assumption does not hold strictly in practical massive MIMO systems because of hardware imperfections such as mutual coupling, cross-polarization leakage, and edge effect.

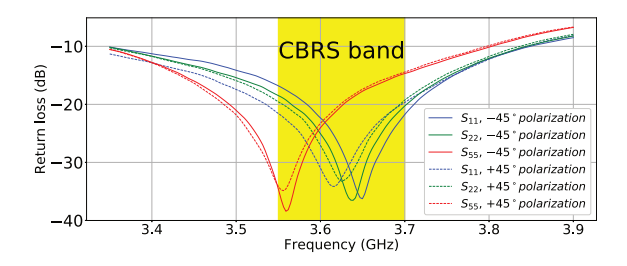


Fig. 3. Measured return loss for a 3×3 antenna array without lenses. Antennas are indexed similarly as depicted in Fig. 1(a). The shaded area corresponds to the CBRS band.

yields over 20 dB isolation between adjacent antenna ports. Multiple measurements were taken using a narrowband signal at 7 different central frequencies, i.e., 3.3 GHz, 3.4 GHz, 3.55 GHz, 3.625 GHz, 3.7 GHz, 3.8 GHz, 3.9 GHz. In all, over 170 measurements were taken. In the rest of this section, we present analysis using measurements from the -45° polarized antenna port with 3.625 GHz central frequency, i.e., the center of the CBRS band.

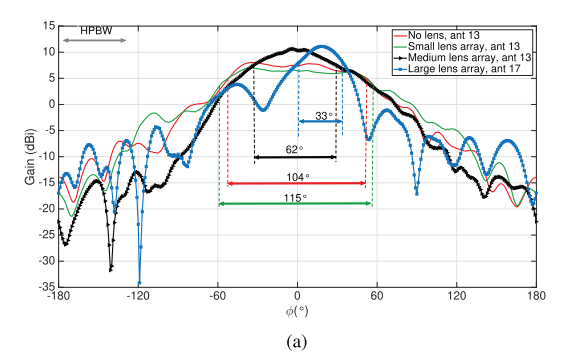
B. Experimental Results

1) Return Loss: We first present the measured return loss (also called reflection coefficient in the literature [49], [50], [51]) for a 3×3 antenna array. The measurements were performed in an anechoic chamber over 3 different antennas with indices 1, 2, and 5 (same indexing method as described previously in Section II-A). For the i-th antenna from the 3×3 antenna array, we refer to its measured return loss as S_{ii} . As depicted in Fig. 3, the measured return loss is at most -14 dB from 3.55 GHz to 3.7 GHz, demonstrating that the patch antenna response adequately spans the CBRS band.

2) Antenna Gain and Directivity: In Fig. 4, we present the measured effective co-polarization beam pattern at the horizontal ($\theta = 90^{\circ}$) and vertical ($\phi = 0^{\circ}$) planes for antenna gain directivity analysis.

For each lens configuration, we present results over one representative antenna from its measurement set S_{ms} , for brevity. For configurations where each single lens covers more than one antenna, the representative antenna was placed near the center of a single lens. More specifically, we present results over antenna 13 for *medium lens array*, and antenna 17 for *large lens array* as they are near the center of the central medium lens, and the bottom left large lens, respectively. The main beam direction of each representing antenna is close to the central direction of $\theta=90^{\circ}, \phi=0^{\circ}$, thus allowing an explicit and fair comparison with each other.

Compared to the baseline configuration of *no lens*, significant directivity enhancement is observed from both *medium lens array* and *large lens array*. As shown in Fig. 4, *medium lens array* reduces the half-power-beamwidth (HPBW) of the measured antenna 13 from approximately 100° to 62° in both elevation and azimuth directions, which also brings a 2.5 dB antenna gain improvement. The optimal performance is observed from *large lens array*, as it further reduces the HPBW to 35° and brings a 7 dB antenna gain improvement. The performance gain



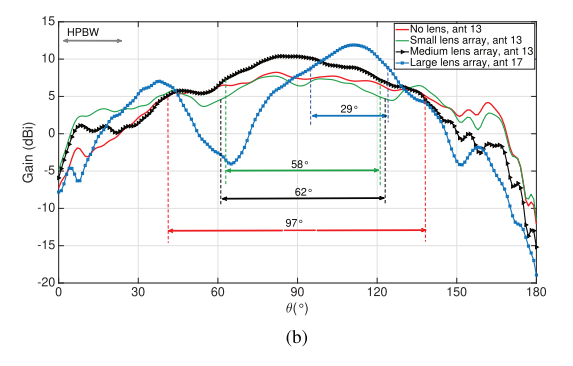


Fig. 4. Measured 3D co-polarization effective beam patterns of representative antennas. For each lens configuration, we choose the representative antenna from near the center of a single lens. (a): horizontal plane (elevation angle $\theta=90^\circ$) slice; (b): vertical plane (azimuth angle $\phi=0^\circ$) slice.

from *large lens array* is also consistent across all measured antennas from its measurement set. As shown in Fig. 5 and Table II, *large lens array* reduces the HPBW of all measured antennas to at most 42° and offers at least 4.5 dB antenna gain improvement. In the case of *small lens array*, the performance gain is at most negligible when compared with the *no lens* baseline.

Due to the spherical symmetry in design, the lenses can passively project the radiated beam toward different 2D directions (both azimuth and elevation) by activating different antennas in the base-station. As is shown in Fig. 5, when no lens or *small lens array* is used, the measured antenna radiates the beam towards approximately the central direction ($\phi = 0^{\circ}, \theta = 90^{\circ}$). In comparison, with lens-enabled effective beam pattern heterogeneity, medium lens array and large lens array can passively project the beam away from the center in both elevation and azimuth directions. As shown in Table II, medium lens array can project the beam away from the center by at most 37° in azimuth (with antenna 12), and 21° in elevation (with antenna 17). And large lens array can further extend this range to 47° in azimuth (with antenna 13) and 50° in elevation (with antenna 12). Such lens-enabled beam direction heterogeneity can be utilized to facilitate cost-effective beamforming solutions [52], [53].

IV. MASSIVE MIMO CHANNEL CHARACTERIZATION

In this section, we study the LensFD resultant massive MIMO full-duplex channels with real-world measurements in both outdoor and indoor environments.

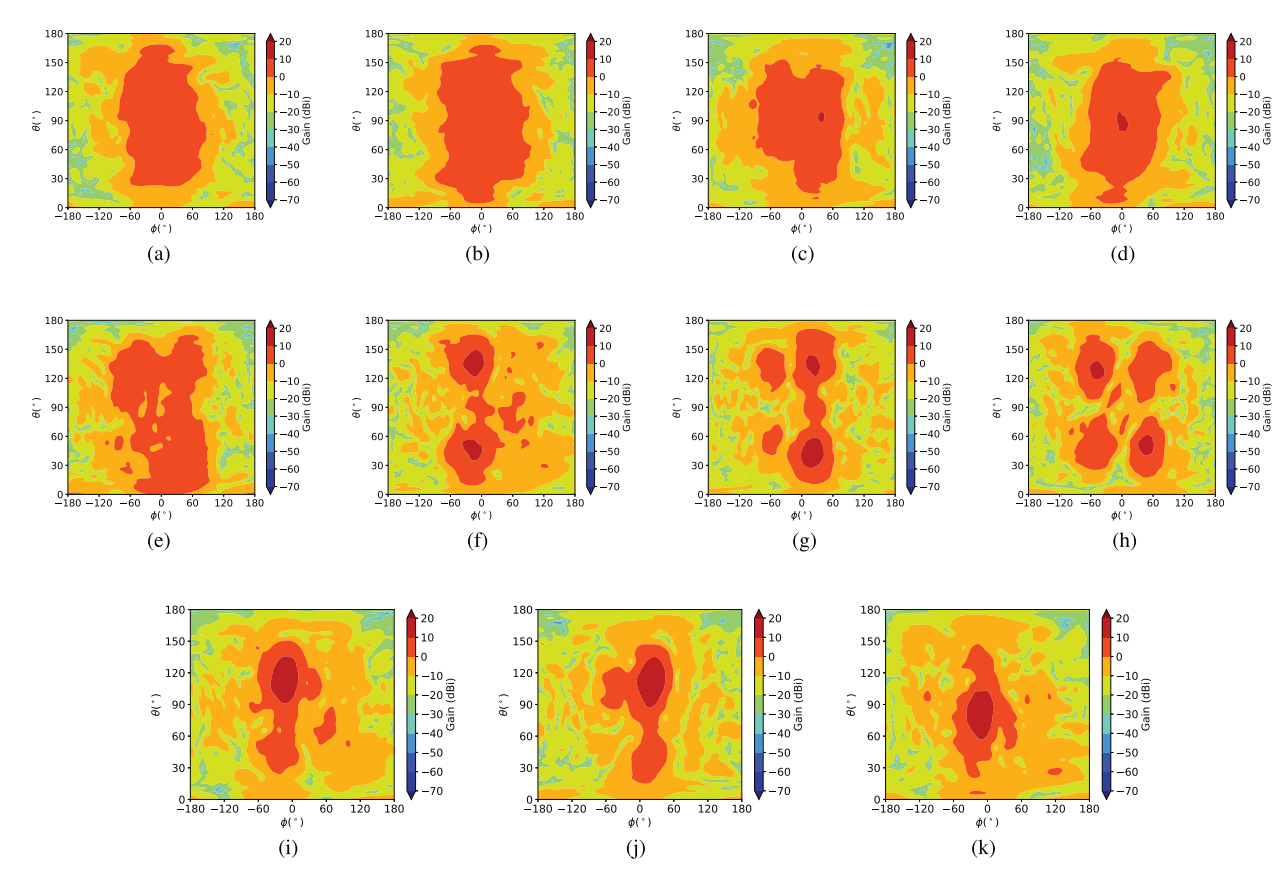


Fig. 5. Measured 3D co-polarization beam patterns for all measured antennas. (a) *No lens*, antenna 13. (b) *Small lens array*, antenna 13. (c) *Medium lens array*, antenna 12. (d) *Medium lens array*, antenna 17. (f) *Large lens array*, antenna 11. (g) *Large lens array*, antenna 12. (h) *Large lens array*, antenna 13. (i) *Large lens array*, antenna 16. (j) *Large lens array*, antenna 17. (k) *Large lens array*, antenna 21.

TABLE II
MAIN CO-POLARIZATION BEAM STATISTICS FOR ALL MEASURED ANTENNAS

Lens configuration	Measured antenna index	Antenna gain (dBi)	Main beam direction	HPBW
no lens	13	8.27	(6°, 83°)	$(104^{\circ}, 97^{\circ})$
small lens array	13	8.04	$(-6^{\circ}, 80^{\circ})$	$(115^{\circ}, 62^{\circ})$
medium lens array	12	10.49	(37°, 94°)	$(36^{\circ}, 72^{\circ})$
	13	10.68	(6°, 85°)	$(62^{\circ}, 58^{\circ})$
	17	9.07	(35°, 69°)	$(30^{\circ}, 28^{\circ})$
large lens array	11	12.78	(-14°, 131°)	$(37^{\circ}, 28^{\circ})$
	12	13.13	$(19^{\circ}, 40^{\circ})$	$(42^{\circ}, 27^{\circ})$
	13	12.32	$(-47^{\circ}, 126^{\circ})$	$(21^{\circ}, 22^{\circ})$
	16	15.23	$(-15^{\circ}, 115^{\circ})$	$(30^{\circ}, 32^{\circ})$
	17	15.33	$(22^{\circ}, 108^{\circ})$	$(33^{\circ}, 35^{\circ})$
	21	15.25	$(-16^{\circ}, 81^{\circ})$	$(39^{\circ}, 37^{\circ})$

For main beam direction and hpbw, we show the value corresponding to the azimuth direction ϕ as the first element in the tuple and the value corresponding to the elevation direction θ as the second.

We first characterize the self-coupling strength (i.e., the power of the self-interference channels, also known as "crosstalk" [54], [55] and "mutual coupling" [56], [57]) between *pairs* of antennas in two different propagation environments - indoor high-scattering and outdoor low-scattering channels.

Our measurement results demonstrate a significant reduction in self-coupling from LensFD in the outdoor but negligible change in the indoor case, thereby supporting the following conclusion. The self-interference power depends on both direct propagation paths between transmit-receive pairs and the backscatter from the environment, and lenses improve when the backscatter is low.

A. Experiment Design

As depicted in Fig. 6, we conducted channel trace measurements in two different propagation environments: a low-scattering outdoor environment in an unoccupied football stadium, and a high-scattering indoor environment inside a building. For each transmission environment, we applied the four lens configurations (as previously introduced at Section III-A, including the baseline of *no lens*) sequentially at the base-station for performance comparison. Measurements of real self-interference and array-to-client channels were collected for each lens configuration and transmission environment using the

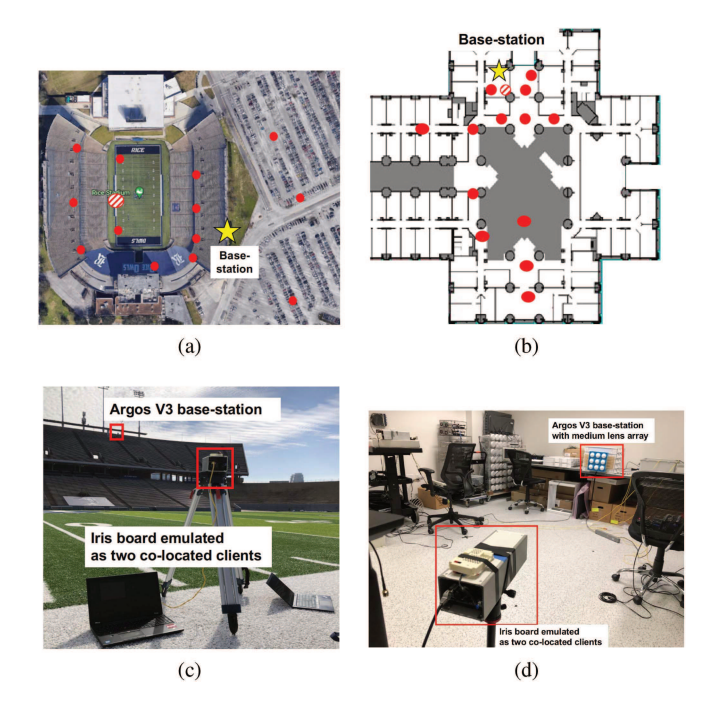


Fig. 6. Experimental setup for LensFD massive MIMO full-duplex channel measurements. (a-b): locations of the base-station and client radios in the outdoor and indoor environment, respectively. The location of each client radio is marked as a red circle. (c-d): example client radio and Faros base-station setup for outdoor and indoor environment, respectively. The location of the example client radio is marked as a red circle with a diagonal pattern in (a) and (b), respectively.

Argos V3/Faros [21], [58], [59] platforms as the base-stations. Two individual base-stations with an identical setup were used in the measurement for the outdoor and indoor environments, and are referred to as the outdoor base-station, and the indoor base-station, respectively. Both the base-stations and the client radios employed custom programmable Software Defined Radio (SDR) modules called Iris board from Skylark Wireless LLC, [60]. Each radio was dual slant linearly polarized and thus provided two independent (±45°) antenna ports. Each Faros base-station consisted of a rectangular UPA array with 80 3.5 GHz patch antennas interfaced to 40 radios. At the basestations, each board was spaced 39.4 mm (approximately halfwavelength in the 3.5 GHz CBRS band) apart in the y-axis and 61.0 mm in the z-axis (see Fig. 7(a) for coordination reference). As illustrated in Fig. 7(a), (b), 6 out of the 40 outdoor base-station radios experienced hardware failure and were not used throughout the measurements, yielding a total of 34 functioning radios in the outdoor base-station. Similarly, 38 functioning radios (i.e., 2 out of 40 experienced hardware failure) were used in the indoor base-station.

For each lens configuration and each transmission environment, we first measured the self-interference channel $\mathbf{H}_S \in \mathbb{C}^{M \times M}$ at the base-station, with M=68 and 76 for the outdoor and the indoor base-stations, respectively. More specifically, we transmitted pilot signals from each base-station antenna in a round-robin fashion, while all other antennas listened to the transmission. We also measured the uplink channel with two

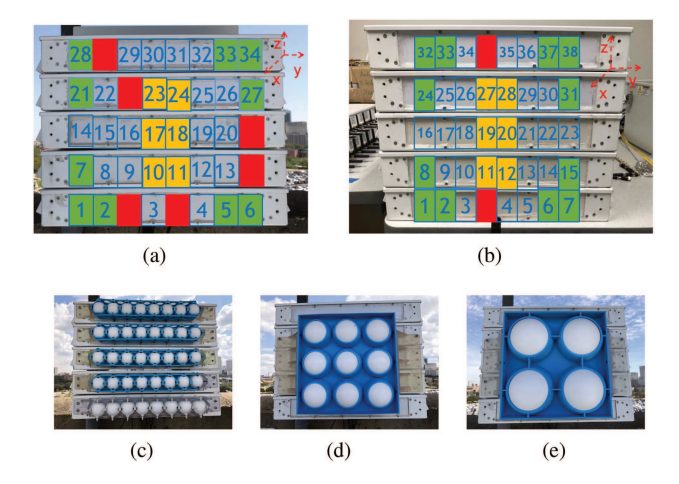


Fig. 7. LensFD massive MIMO base-station with Faros platform. (a-b): indexes of functioning dual-polarized radios in the outdoor and indoor base-stations, respectively. The radios experiencing a hardware failure are marked as red and were not used in the measurement. The central and corner radios are marked in yellow and green rectangles, respectively. Compared to the central radios, the corner radios have a longer average distance to the other radios. (c-e): outdoor base-station equipped with *small lens array*, *medium lens array*, and *large lens array*, respectively. A similar installation strategy was applied to the indoor base-station as well. (a) Outdoor base-station. (b) Indoor base-station. (c) *Small lens array*. (d) *Medium lens array*. (e) *Large lens array*.

co-located clients emulated by two antennas interfaced to a single dual-polarized client radio. For each given location as shown in Fig. 6, we collected uplink channel traces by transmitting pilot signals from the two client antennas to the base-station. Note that when measuring the array-to-client channel for clients located outside the stadium (see illustration in Fig. 6(a)), we rotated the base-station by 180° , allowing it to face toward these client locations. For each lens configuration and transmission environment, the uplink channel $\mathbf{H}_U \in \mathbb{C}^{M \times K_u}$ with $K_u = 28$ is generated by combining measurements from the 14 different locations as shown in Fig. 6. Since TDD transmission was employed throughout the measuring process, channel reciprocity can be leveraged to easily obtain the downlink channel as $\mathbf{H}_D = \mathbf{H}_U^T$.

For each channel measurement, the channel state information (CSI) values were collected at 3.6 GHz central frequency in a 5 MHz bandwidth. We used the Sounder tool from the RENEW [61] platform to continuously transmit 400 frames (for a total time of approximately 3.5 seconds) of the pilot signal from each transmit antenna to the receiving antenna. Both the base-station and the clients supported OFDM transmission. More precisely, the 5 MHz bandwidth was further divided into 64 OFDM subcarriers, 52 of which were utilized during the measurement. In all, more than 100 GB of data were collected and released to public. More details of the channel measurement and signal processing process can be found in [21].

B. Experimental Results

Result 1: The real-world performance gain from LensFD depends heavily on the transmission environment. For a typical outdoor environment with limited reflection, LensFD can provide an additional 4–7 dB suppression in self-coupling strength.

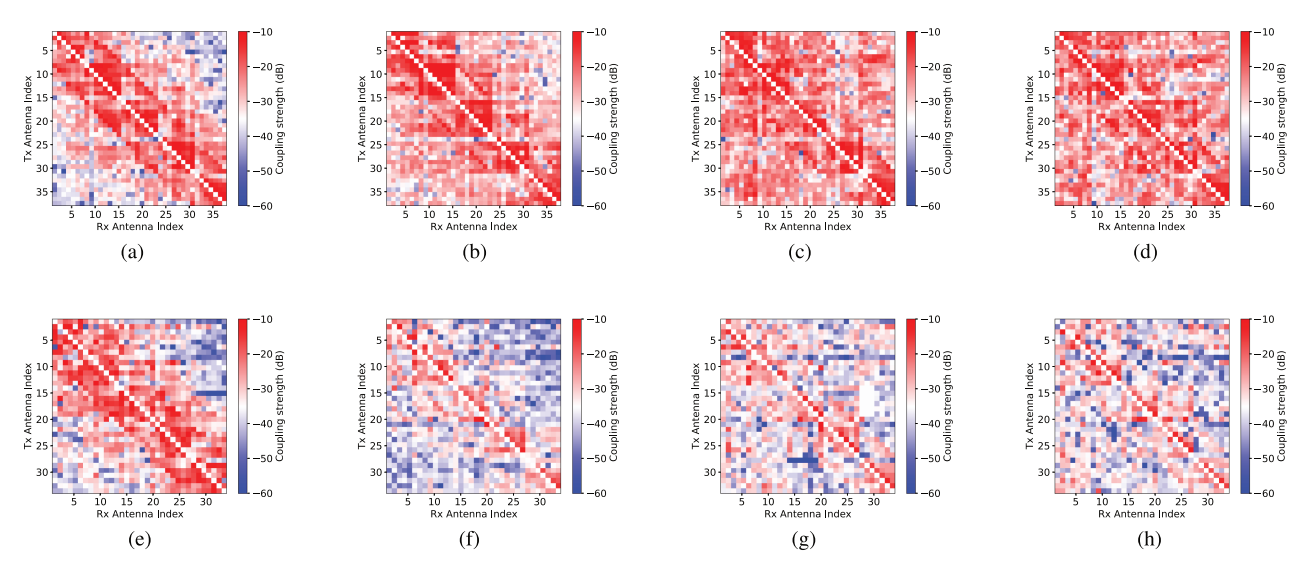


Fig. 8. Self-coupling strength at the base-station. (a) Indoor, *no lens*. (b) Indoor, *small lens array*. (c) Indoor, *medium lens array*. (d) Indoor, *large lens array*. (e) Outdoor, *no lens*. (f) Outdoor, *small lens array*. (g) Outdoor, *medium lens array*. (h) Outdoor, *large lens array*.

TABLE III
STATISTICS OF MEASURED LENSFD RESULTANT MASSIVE MIMO
SELF-INTERFERENCE CHANNELS IN BOTH OUTDOOR
AND INDOOR ENVIRONMENTS

	Self-coupling strength (dB)				
Lens configuration	central radios		corner radios		
	outdoor	indoor	outdoor	indoor	
no lens	-25.97	-26.67	-32.27	-30.01	
small lens array	-34.89	-26.52	-37.51	-26.72	
medium lens array	-33.00	-24.12	-35.35	-24.66	
large lens array	-34.78	-24.41	-35.83	-25.17	

We show the median self-coupling strength transmitted from the central and corner radios (illustration in Fig. 7) to all the functioning radios, respectively.

On the contrary, the performance gain from LensFD in the indoor environment with rich reflection is limited to none, e.g., using lenses even strengthens the self-coupling strength by 1–5 dB.

We first examine the self-coupling strength at the base-station. Shown in Fig. 8 is the self-coupling strength between all -45° polarized antennas in the base-station. The color of each element (i,j) in Fig. 8 denotes the average self-coupling strength from transmit antenna i to receive antenna j over 400 frames, where the antennas are indexed row-wise as shown in Fig. 7. Note that we only show the self-coupling between distinct antennas (i.e., $i\neq j$) since the radios we used do not support reflection coefficient measurements, and thus the empty anti-diagonal elements. In addition, we only show the co-polarization self-coupling result with -45° polarized antenna for each dual-polarized radio, allowing us to eliminate the effect of cross-polarization self-coupling suppression from LensFD performance analysis.

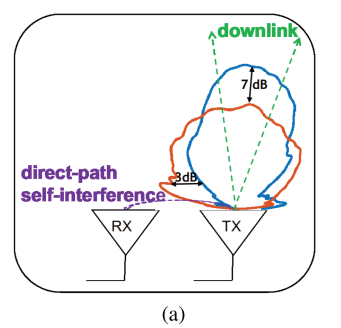
As shown in Fig. 8 and Table III, there is significant variation in the self-coupling strength among all the antenna pairs. We summarize three major parameters in determining the self-coupling strength in LensFD as follows:

Antenna distance: Antenna pairs with shorter distance typically yield stronger self-coupling strength. Such dependence

can be well explained by the difference in the direct-path selfcoupling strength as it is inversely proportional to the square of the transmission distance. Using the outdoor measurement with no lens in Fig. 8(e) as an example, while antennas adjacent to each other can have a self-coupling as strong as -10 dB, the self-coupling strength for antennas far apart can fall below -50 dB. In Table III we report the self-coupling strength received by the central radios and the corner radios. Given the UPA structure of the base-stations, the average distance from the corner radios to the other radios is $1.6 \times$ the distance from the center radios to the other radios. Such difference in transmission distance is well manifested in their difference in self-coupling strength. For each fixed lens configuration and transmission environment evaluated, the median self-coupling strength at the corner radios is 0-5 dB lower compared to that of the central radios.

Transmission environment: For each given antenna pair, the self-coupling strength in indoor environments is typically stronger than the outdoor self-coupling strength, especially when the transmit and receive antennas are far from each other. As shown in Table III, for central radios the median self-coupling strength in the indoor environment is 1–10 dB stronger than that of the outdoor environment for all lens configurations. As for the corner radios with longer average antenna pair distance, we observe a larger gap of 3–11 dB between the indoor and outdoor environments. The increased self-coupling in indoor environment typically has a much richer scattering: the indoor environment typically has a much richer scattering profile. For the antenna pairs far from each other, the self-coupling from backscattering is comparable or even stronger compared to the direct-path self-coupling [44], [62].

Lenses: The effect from lenses over the self-coupling strength depends on the transmission environment: for the outdoor environment, the lenses suppress the self-coupling strength (see the comparison in Fig. 8(e-h)); while for the indoor environment, the lenses strengthen the self-coupling (see the comparison in



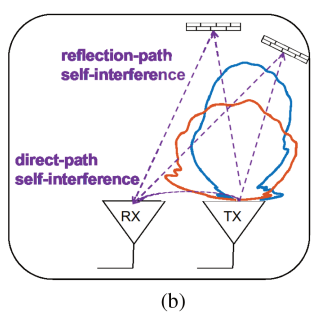


Fig. 9. Beam reshaping effect of LensFD in different transmission environments. Measurement-based effective beam patterns corresponding to *no lens* and *large lens array* are drawn in orange and blue, respectively. (a): downlink and self-interference channel paths in a typical outdoor environment with limited reflection path. (b): direct-path and reflection-path self-interference channel in a typical indoor environment with rich reflection sources. The downlink channel paths are similar to those shown in the outdoor environment of (a) and are thus emitted for brevity. (a) Outdoor. (b) Indoor.

Fig. 8(a–d)). As shown in Table III, using lenses in the outdoor environment provides an additional 4–7 dB suppression in self-coupling power, which serves as the key enabler of using LensFD to improve massive MIMO full-duplex performance. We also report that when using lenses in the indoor environment, the self-coupling power was strengthened by 1–5 dB.

The effect of antenna distance and transmission environment was previously reported and explained in [44], [62], and we complete this picture by adding the effect of lenses as it is the key enabler of LensFD.

We provide a first-order analysis of LensFD's performance and its dependency on the transmission environment (i.e., the multipath richness) as follows. For a typical UPA-structured massive MIMO base-station, the direct path for the selfinterference channel is generally outside the base-station's broadside, which allows LensFD to effectively suppress its power as illustrated in Fig. 9. In a typical outdoor scenario with a limited number of reflection paths, the self-interference channel is dominated by the direct path. In this case, the self-interference channel power is effectively suppressed as the direct path power is suppressed in LensFD. In comparison, with a stronger and richer multipath reflection, the self-interference channel is no longer dominated by the direct path. As illustrated in Fig. 9, the reflection paths typically correspond to AoA and AoD from within the broadside of the transmit and receive antenna, thus having comparable or even stronger power compared to the direct path in self-interference. Similar to the uplink and downlink signal, sub-channels corresponding to these reflection paths are also strengthened due to the beam reshaping effect of LensFD, thus the desired suppressing effect over the combined self-interference channel quickly diminishes to negligible, if not even worse.

It's worth noticing that the per-antenna measurements are not sufficient to predict which size lens-array performs the best. For example, in Section III *large lens array* yields the highest antenna gain of 7 dB and improved directivity. In comparison,

the gain from *small lens array* is negligible to none. However, here in the massive MIMO channel measurements, we observe that *small lens array* in turn yields optimal performance with the highest amount of self-coupling suppression. This illustrates that, it's not sufficient to use per-antenna beam pattern measurements to predict lens' full-duplex performance as self-interference in a UPA depends on interference from multiple antennas and lens shape self-interference from different transmit antennas in a complex manner. For instance, as we see in Fig. 5, *large lens array* shapes patterns in rather complex manner, and hence metrics like beamwidth and antenna gain are less meaningful to predict self-coupling.

V. MASSIVE MIMO FULL-DUPLEX EVALUATION

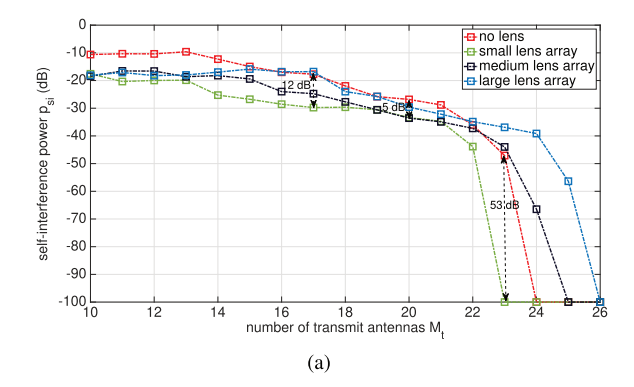
In Section IV we used massive MIMO channel measurements to show that by using lenses, LensFD can reduce the self-interference strength by 4–7 dB in a typical outdoor environment. To push forward the full-duplex performance, LensFD combines a digital precoder with a lens array to achieve significant overall self-interference reduction. Several precoder-based self-interference suppression algorithms have been proposed, e.g. SoftNull [13] and JointNull [12]. LensFD can be used with any of the existing precoding methods. We will use JointNull [12] as a representative precoder since it jointly optimizes downlink beamforming and self-interference suppression, and can be easily adapted with systems using lenses.

A. Experiment Design

We analyze LensFD performance in massive MIMO fullduplex operations with real-world measurements from Section IV. For the purpose of eliminating the effect of crosspolarization self-coupling suppression, we only use the -45° polarized antenna for both base-station and the client radios. Note that to provide sufficient downlink degrees-of-freedom, i.e., the number of dimensions available for downlink transmission, the base-station needs to have at least the same amount of transmit antennas as the number of downlink clients [12], [13]. Since the precoder-based methods partition into transmit and receive sub-arrays, and then further devote some of the transmit degrees-of-freedom for self-interference cancellation, the number of clients that can be supported is less than full-array systems. Thus, we study a maximum of 20 client locations, i.e., $K_d = K_u = 10$, for both outdoor and indoor cases. We adopt a similar analysis approach as [12] and focus on the comparison between different lens configurations.

B. Main Results

Result 2: For a fixed downlink receive power, LensFD consistently yields more self-interference suppression over no lens in the outdoor case. Specifically, small lens array consistently outperforms all lens configurations in the outdoor system. However, LensFD provides little to no lensing gains in the indoor case.



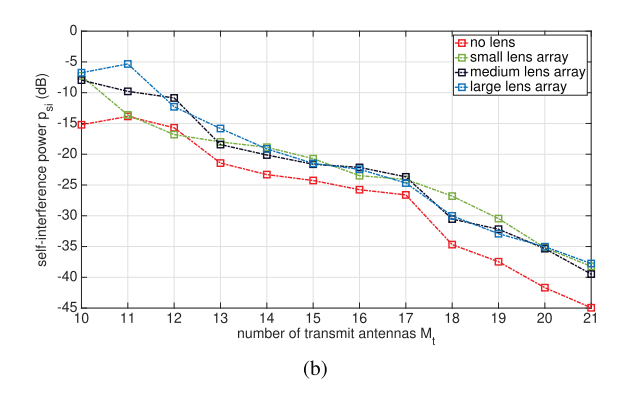


Fig. 10. Self-interference power using JointNull with fixed downlink receive power $p_{dl} = -75$ dB. For each M_t , we present results using the transceiver configuration that yields maximum uplink power p_{ul} . Self-interference power from $no\ lens$ with no digital precoding is used as the 0 dB baseline. (a) Outdoor. (b) Indoor.

Note that in Result 2, we fix the downlink receive power and then optimize the digital precoder for each lens configuration. This ensures that in each case, the downlink performance is the same, thereby allowing fair comparisons.

In Fig. 10 we present the self-interference power p_{si} with different number of transmit antennas M_t . We use self-interference power measured from $no\ lens$ and no digital precoding as the 0 dB baseline and assume a -100 dB noise floor. For each M_t , there exist several transceiver configurations that facilitate self-interference suppression (more details in [12]). Each configuration has M_t transmit antennas and $M_r = M - M_t$ receive antennas, but differ from each other in which M_t antennas are selected for transmitting. For each M_t , we fix the downlink receive power to be -75 dB and calculate the corresponding uplink power p_{ul} for each configuration. We present the results using the optimal configuration with the highest uplink power in Fig. 10.

We first analyze the result for the outdoor environment in Fig. 10(a) where using lenses helps suppress self-interference power. Note that all cases can suppress self-interference to near zero for certain M_t where there are sufficient degrees-of-freedom available. We first cast our eyes to the region before nulling self-interference, that is, $M_t \leq 22$ for all lens configurations. In this region, $no\ lens$ only enjoys a digital precoding gain from JointNull and the overall self-interference suppression is limited to 10-35 dB. By adding a lensing gain, LensFD pushes

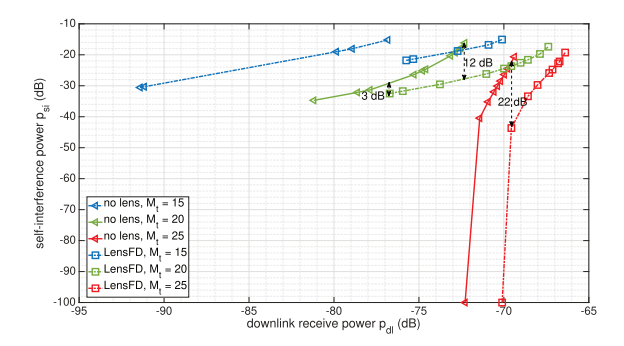


Fig. 11. Self-interference and downlink receive power tradeoff curves for *small lens array* with three different transceiver configurations. We show results from the outdoor environment and use self-interference power from *no lens* with no digital precoding as the 0 dB baseline.

forward the self-interference suppression to 15–44 dB. *small lens array* consistently yields optimal performance as it provides 5–12 dB additional self-interference suppression as compared to *no lens*. In comparison, the lensing gain from *large lens array* is limited to at most 5 dB over *no lens* before nulling self-interference. The difference in lensing gain across different lens configurations is consistent with the self-coupling strength analysis in Section IV.

In regions where self-interference can be suppressed to near zero, small lens array also outperforms no lens as it requires fewer downlink degrees-of-freedom with $M_t=22$, as compared to $M_t=23$ for no lens. The saved downlink degrees-of-freedom can be used in small lens array for downlink capacity improvement.

In Fig. 10(b) we observe that in a typical indoor environment, using lenses can hurt the full-duplex performance by increasing self-interference power to the system, which is also consistent with the analysis in Section IV. In the remainder of this section, we omit relevant analysis of the indoor environment and focus on the outdoor measurement results where a lensing gain is available in LensFD.

Result 3: LensFD improves the tradeoff between downlink power and self-interference suppression, compared to no lens system.

In Fig. 11, we show the tradeoff for *small lens array*, which is the optimal lens configuration for self-interference suppression as shown in Fig. 10. For all transceiver configurations analyzed in Fig. 11, LensFD significantly improves the tradeoff between downlink received power and self-interference power. For example, with $M_t=20$ (and thus $M_r=M-M_t=14$), LensFD provides 3-12 dB additional self-interference suppression compared to *no lens*. For a more asymmetric system with more transmit antennas (more practical in real-world deployments) as $M_t=20$, LensFD performance gain over *no lens* is pushed forward to 22 dB before nulling self-interference to near zero.

Result 4: In the outdoor environment, LensFD provides achievable rate gain in both uplink and downlink, yielding at most $1.6 \times$ sum-rate gain over the baseline of TDD with no lens.

In Fig. 12 we show the achievable rates for a continuum of uplink-downlink rate power pairs for the outdoor case. We show

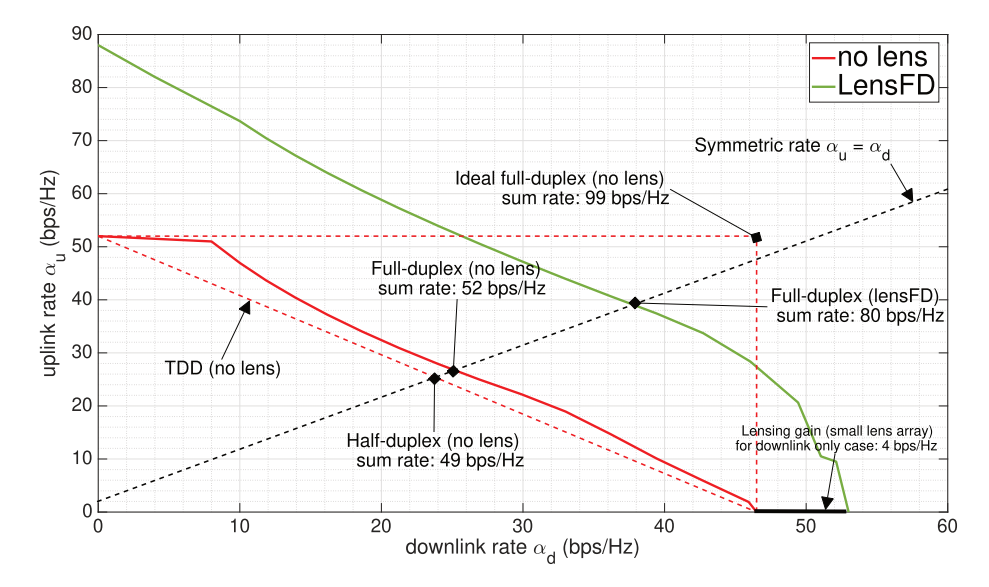


Fig. 12. Achievable rate comparison across different lens configurations in the outdoor environment. The solid lines correspond to the achievable rate of each lens configuration with JointNull precoder. The anti-diagonal red dashed line is the half-duplex (TDD) rate with no lens, and the horizontal and vertical ones are the corresponding ideal full-duplex rate. The black diagonal dashed line corresponds to the symmetric sum-rate, i.e., $\alpha_u = \alpha_d$.

that compared to the half-duplex baseline with *no lens*, LensFD with *small lens array* offers a $1.6 \times$ symmetric sum-rate (i.e., $\alpha = 2\alpha_u = 2\alpha_d$) improvement. The $1.6 \times$ sum-rate gain constitutes two gains: *duplexing gain* and the *lensing gain*.

The duplexing gain is achieved by operating the base-station in a full-duplex mode and using only the digital precoder to suppress self-interference, much like past methods. As shown in Fig. 12, for *no lens* the duplexing gain is 3 bps/Hz as it improves the sum-rate from 49 bps/Hz (TDD) to 52 bps/Hz (full-duplex).

The lensing gain comes from additional self-interference suppression due to the beam reshaping effect unique to LensFD. As shown in Fig. 11 and 10, *small lens array* consistently provides additional self-interference power suppression while maintaining the same amount of downlink and uplink power. This translates into an extra rate gain, that pushes the overall gain to 80 bps/Hz, $1.5 \times$ the sum-rate of *no lens* in full-duplex mode, or $1.6 \times$ the sum-rate of the baseline scenario with no lens in TDD mode. As shown in Fig. 12, using *small lens array* with the JointNull precoder yields a maximum sum-rate of 80 bps/Hz. We highlight that lensing gain manifests throughout the rate region. For example, both downlink-only and uplink-only rate points (i.e., no full-duplex points) achieve a rate gain. That gain comes from the fact that lenses increase the antenna main-lobe gain by reducing side-lobes, which benefits both uplink and downlink, even without full-duplex operation.

VI. CONCLUSION

In this paper, we presented LensFD, a scalable method that uses a dielectric lens array to improve the performance of sub-6 GHz massive MIMO full-duplex systems. The most attractive aspect of LensFD is that its performance improvement can be achieved potentially *post*-deployment for any system that attentively adjusts its self-interference suppression based on measurements. The proposed dielectric spherical lens arrays in LensFD

are cost-effective in the design and fabrication process and can be easily installed mechanically over the existing UPA-structured massive MIMO setup. One possible extension of this work is to jointly optimize the system's performance in full-duplex operations by co-design of the antenna and lens array at the base-station. We also plan to develop a beam-pattern-dependent antenna array partition algorithm in future work such that the base-station can intelligently partition the antenna array into transmitting and receiving antennas based on the reshaped beam pattern of each antenna.

ACKNOWLEDGMENT

The authors would like to thank Kevin Linehan from Comm-Scope, Dr. Ryan Guerra, Bryan Grandy, John Harris and Sharan Erukulla from Skylark Wireless, Hang Wang and Dr. Taiyun Chi from Rice University Electrical and Computer Engineering department for their support throughout the project.

REFERENCES

- E. G. Larsson, O. Edfors, F. Tufvesson, and T. L. Marzetta, "Massive MIMO for next generation wireless systems," *IEEE Commun. Mag.*, vol. 52, no. 2, pp. 186–195, Feb. 2014.
- [2] T. L. Marzetta, "Massive MIMO: An introduction," Bell Labs Tech. J., vol. 20, pp. 11–22, 2015.
- [3] X. Artiga, J. Perruisseau-Carrier, and A. I. Pérez-Neira, "Antenna array configurations for massive MIMO outdoor base stations," in *IEEE 8th Sensor Array Multichannel Signal Process. Workshop*, 2014, pp. 281–284.
- [4] J. R. Pêrez, R. P. Torres, M. Domingo, L. Valle, and J. Basterrechea, "Analysis of massive MIMO performance in an indoor picocell with high number of users," *IEEE Access*, vol. 8, pp. 107025–107034, 2020.
- [5] S. Rajoria, A. Trivedi, and W. W. Godfrey, "A comprehensive survey: Small cell meets massive MIMO," *Phys. Commun.*, vol. 26, pp. 40–49, 2018. [Online]. Available: https://www.sciencedirect.com/science/article/pii/S187449071730112X
- [6] E. Björnson, J. Hoydis, and L. Sanguinetti, "Massive MIMO has unlimited capacity," *IEEE Trans. Wireless Commun.*, vol. 17, no. 1, pp. 574–590, Jan. 2018.

- [7] K. N. R. S. V. Prasad, E. Hossain, and V. K. Bhargava, "Energy efficiency in massive MIMO-based 5G networks: Opportunities and challenges," *IEEE Wireless Commun.*, vol. 24, no. 3, pp. 86–94, Jun. 2017.
- [8] E. Björnson, L. Sanguinetti, J. Hoydis, and M. Debbah, "Designing multiuser MIMO for energy efficiency: When is massive MIMO the answer?," in *Proc. IEEE Wireless Commun. Netw. Conf.*, 2014, pp. 242–247.
- [9] E. Björnson, E. G. Larsson, and T. L. Marzetta, "Massive MIMO: Ten myths and one critical question," *IEEE Commun. Mag.*, vol. 54, no. 2, pp. 114–123, Feb. 2016.
- [10] V. K. Garg, IS-95 CDMA and CDMA2000: Cellular/PCS Systems Implementation. London, U.K.: Pearson Educ., 1999.
- [11] H. Kaaranen, A. Ahtiainen, L. Laitinen, S. Naghian, and V. Niemi, UMTS Networks: Architecture, Mobility and Services. Hoboken, NJ, USA: Wiley, 2005
- [12] N. M. Gowda and A. Sabharwal, "JointNull: Combining partial analog cancellation with transmit beamforming for large-antenna full-duplex wireless systems," *IEEE Trans. Wireless Commun.*, vol. 17, no. 3, pp. 2094–2108, Mar. 2018.
- [13] E. Everett, C. Shepard, L. Zhong, and A. Sabharwal, "SoftNull: Many-antenna full-duplex wireless via digital beamforming," *IEEE Trans. Wireless Commun.*, vol. 15, no. 12, pp. 8077–8092, Dec. 2016.
- [14] M. Duarte and A. Sabharwal, "Full-duplex wireless communications using off-the-shelf radios: Feasibility and first results," in *Proc. Conf. Rec. 44th Asilomar Conf. Signals Syst. Comput.*, 2010, pp. 1558–1562.
- [15] M. Duarte, C. Dick, and A. Sabharwal, "Experiment-driven characterization of full-duplex wireless systems," *IEEE Trans. Wireless Commun.*, vol. 11, no. 12, pp. 4296–4307, Dec. 2012.
- [16] J. I. Choi, M. Jain, K. Srinivasan, P. Levis, and S. Katti, "Achieving single channel, full duplex wireless communication," in *Proc. 16th Annu. Int. Conf. Mobile Comput. Netw.*, 2010, pp. 1–12.
- [17] 3rd Generation Partnership Project (3GPP), "Study on scenarios and requirements for next generation access technologies," 3GPP, Sophia Antipolis, France, Tech. Rep. 38.913 V14.1.0, 2017.
- [18] R. Chataut and R. Akl, "Massive MIMO systems for 5G and beyond networks—overview, recent trends, challenges, and future research direction," Sensors, vol. 20, no. 10, 2020, Art. no. 2753.
- [19] A. Sahai, G. Patel, and A. Sabharwal, "Pushing the limits of full-duplex: Design and real-time implementation," Rice Univ., Houston, TX, USA, Tech. Rep. TREE1104, 2011.
- [20] A. Sabharwal, P. Schniter, D. Guo, D. W. Bliss, S. Rangarajan, and R. Wichman, "In-band full-duplex wireless: Challenges and opportunities," *IEEE J. Sel. Areas Commun.*, vol. 32, no. 9, pp. 1637–1652, Sep. 2014.
- [21] C. Shepard, J. Ding, R. E. Guerra, and L. Zhong, "Understanding real many-antenna MU-MIMO channels," in *Proc. IEEE 50th Asilomar Conf. Signals Syst. Comput.*, 2016, pp. 461–467.
- [22] M. Jain et al., "Practical, real-time, full duplex wireless," in Proc. 17th Annu. Int. Conf. Mobile Comput. Netw., 2011, pp. 301–312.
- [23] D. Bharadia, E. McMilin, and S. Katti, "Full duplex radios," in *Proc. ACM SIGCOMM 2013 Conf. SIGCOMM*, 2013, pp. 375–386.
- [24] A. T. Le, L. C. Tran, X. Huang, and Y. J. Guo, "Beam-based analog self-interference cancellation in full-duplex MIMO systems," *IEEE Trans. Wireless Commun.*, vol. 19, no. 4, pp. 2460–2471, Apr. 2020.
- [25] X. Huang, A. T. Le, and Y. J. Guo, "Transmit beamforming for communication and self-interference cancellation in full duplex MIMO systems: A trade-off analysis," *IEEE Trans. Wireless Commun.*, vol. 20, no. 6, pp. 3760–3769, Jun. 2021.
- [26] D. W. Bliss, P. A. Parker, and A. R. Margetts, "Simultaneous transmission and reception for improved wireless network performance," in *Proc.* IEEE/SP 14th Workshop Stat. Signal Process. 2007, pp. 478–482.
- [27] J. Sangiamwong, T. Asai, J. Hagiwara, Y. Okumura, and T. Ohya, "Joint multi-filter design for full-duplex MU-MIMO relaying," in *Proc. IEEE* 69th Veh. Technol. Conf., 2009, pp. 1–5.
- [28] Y. Zeng, R. Zhang, and Z. N. Chen, "Electromagnetic lens-focusing antenna enabled massive MIMO: Performance improvement and cost reduction," *IEEE J. Sel. Areas Commun.*, vol. 32, no. 6, pp. 1194–1206, Jun. 2014.
- [29] Y. Zeng and R. Zhang, "Cost-effective millimeter-wave communications with lens antenna array," *IEEE Wireless Commun.*, vol. 24, no. 4, pp. 81–87, Aug. 2017.
- [30] J. Brady, N. Behdad, and A. M. Sayeed, "Beamspace MIMO for millimeter-wave communications: System architecture, modeling, analysis, and measurements," *IEEE Trans. Antennas Propag.*, vol. 61, no. 7, pp. 3814–3827, Jul. 2013.
- [31] Y. J. Cho, G.-Y. Suk, B. Kim, D. K. Kim, and C.-B. Chae, "RF lensembedded antenna array for mmwave MIMO: Design and performance," *IEEE Commun. Mag.*, vol. 56, no. 7, pp. 42–48, Jul. 2018.

- [32] A. Artemenko, A. Maltsev, A. Mozharovskiy, A. Sevastyanov, V. Ssorin, and R. Maslennikov, "Millimeter-wave electronically steerable integrated lens antennas for WLAN/WPAN applications," *IEEE Trans. Antennas Propag.*, vol. 61, no. 4, pp. 1665–1671, Apr. 2013.
- [33] D. F. Filipovic, G. P. Gauthier, S. Raman, and G. M. Rebeiz, "Off-axis properties of silicon and quartz dielectric lens antennas," *IEEE Trans. Antennas Propag.*, vol. 45, no. 5, pp. 760–766, May 1997.
- [34] K. Haneda, J. Järveläinen, A. Karttunen, and J. Putkonen, "Self-interference channel measurements for in-band full-duplex street-level backhaul relays at 70 GHz," in *Proc. IEEE 29th Annu. Int. Symp. Pers. Indoor and Mobile Radio Commun.*, 2018, pp. 199–204.
- [35] T. Li and Z. N. Chen, "Compact wideband wide-angle polarization-free metasurface lens antenna array for multibeam base stations," *IEEE Trans. Antennas Propag.*, vol. 68, no. 3, pp. 1378–1388, Mar. 2020.
- [36] S. Li, Z. N. Chen, T. Li, F. H. Lin, and X. Yin, "Characterization of metasurface lens antenna for sub-6 GHz dual-polarization full-dimension massive MIMO and multibeam systems," *IEEE Trans. Antennas Propag.*, vol. 68, no. 3, pp. 1366–1377, Mar. 2020.
- [37] E. A. Etellisi, M. A. Elmansouri, and D. S. Filipović, "In-band full-duplex multimode lens-loaded eight-arm spiral antenna," *IEEE Trans. Antennas Propag.*, vol. 66, no. 4, pp. 2084–2089, Apr. 2018.
- [38] K. E. Linehan, "Lensed antennas for use in wireless communications systems," U.S. Patent 10,959,110, Mar. 23, 2021.
- [39] M. Zimmerman, I. Timofeev, and K. E. Linehan, "Lensed antennas for use in cellular and other communications systems," U.S. Patent 10,483, 650B1, Nov. 19, 2019.
- [40] Q. Gao, G. Chen, L. Liao, and Y. Hua, "Full-duplex cooperative transmission scheduling in fast-fading MIMO relaying wireless networks," in Proc. Int. Conf. Comput. Netw. Commun., 2014, pp. 771–775.
- [41] C. Karakus and S. Diggavi, "Opportunistic scheduling for full-duplex uplink-downlink networks," in *Proc. IEEE Int. Symp. Inf. Theory*, 2015, pp. 1019–1023.
- [42] S. Shahsavari, D. Ramirez, and E. Erkip, "Joint user scheduling and power optimization in full-duplex cells with successive interference cancellation," in 51st Asilomar Conf. Signals, Systems, Comput., 2017, pp. 1099–1104.
- [43] B. Li, C. Li, C. Yang, and B. Xia, "User scheduling for full-duplex cellular networks," in *Proc. IEEE Int. Conf. Commun. Workshops*, 2019, pp. 1–6.
- [44] A. Tang and X. Wang, "A-duplex: Medium access control for efficient coexistence between full-duplex and half-duplex communications," *IEEE Trans. Wireless Commun.*, vol. 14, no. 10, pp. 5871–5885, Oct. 2015.
- [45] J. Y. Kim, O. Mashayekhi, H. Qu, M. Kazandjieva, and P. Levis, "Janus: A novel MAC protocol for full duplex radio," Dept. Comput. Sci., Stanford Univ., Stanford, CA, USA, Tech. Rep. CSTR 2013-02, Jul. 2013.
- [46] NSI-MI. Accessed: Feb. 11, 2023. [Online]. Available: https://www.nsi-mi.com/
- [47] Q. Liao, N. J. G. Fonseca, and O. Quevedo-Teruel, "Compact multibeam fully metallic geodesic Luneburg lens antenna based on non-Euclidean transformation optics," *IEEE Trans. Antennas Propag.*, vol. 66, no. 12, pp. 7383–7388, Dec. 2018.
- [48] O. Quevedo-Teruel, J. Miao, M. Mattsson, A. Algaba-Brazalez, M. Johansson, and L. Manholm, "Glide-symmetric fully metallic Luneburg lens for 5G communications at ka-band," *IEEE Antennas Wireless Propag. Lett.*, vol. 17, no. 9, pp. 1588–1592, Sep. 2018.
- [49] J. Ala-Laurinaho et al., "2-D beam-steerable integrated lens antenna system for 5G E-band access and backhaul," *IEEE Trans. Microw. Theory Techn.*, vol. 64, no. 7, pp. 2244–2255, Jul. 2016.
- [50] X. Chen and P.-S. Kildal, "Accuracy of antenna input reflection coefficient and mismatch factor measured in reverberation chamber," in *Proc. 3rd Eur. Conf. Antennas Propag.*, 2009, pp. 2678–2681.
- [51] D. Hill, "A reflection coefficient derivation for the Q of a reverberation chamber," *IEEE Trans. Electromagn. Compat.*, vol. 38, no. 4, pp. 591–592, Nov. 1996.
- [52] A. Abbaspour-Tamijani, L. Zhang, G. Pan, H. K. Pan, and H. Alavi, "Lens-enhanced phased array antenna system for high directivity beam-steering," in *Proc. IEEE Int. Symp. Antennas Propag.*, 2011, pp. 3275–3278.
- [53] R. Xu and Z. N. Chen, "A compact beamsteering metasurface lens array antenna with low-cost phased array," *IEEE Trans. Antennas Propag.*, vol. 69, no. 4, pp. 1992–2002, Apr. 2021.
- [54] J. Ma, G. Y. Li, J. Zhang, T. Kuze, and H. Iura, "A new coupling channel estimator for cross-talk cancellation at wireless relay stations," in *Proc. IEEE Glob. Telecommun. Conf.*, 2009, pp. 1–6.
- [55] N. Miura, D. Mizoguchi, T. Sakurai, and T. Kuroda, "Cross talk countermeasures in inductive inter-chip wireless superconnect," in *Proc. IEEE Custom Integr. Circuits Conf.*, 2004, pp. 99–102.

- [56] J. W. Wallace and M. A. Jensen, "Mutual coupling in MIMO wireless systems: A rigorous network theory analysis," *IEEE Trans. Wireless Commun.*, vol. 3, no. 4, pp. 1317–1325, Jul. 2004.
- [57] S. Raju, R. Wu, M. Chan, and C. P. Yue, "Modeling of mutual coupling between planar inductors in wireless power applications," *IEEE Trans. Power Electron.*, vol. 29, no. 1, pp. 481–490, Jan. 2014.
- [58] C. W. Shepard, R. Doost-Mohammady, R. E. Guerra, and L. Zhong, "Argos V3: An efficient many-antenna platform," in *Proc. 23rd Annu. Int. Conf. Mobile Comput. Netw.*, 2017, pp. 501–503.
- [59] C. Shepard, R. Doost-Mohammady, J. Ding, R. E. Guerra, and L. Zhong, "ArgosNet: A multi-cell many-antenna MU-MIMO platform," in *Proc. 52nd Asilomar Conf. Signals, Syst., Comput.*, 2018, pp. 2237–2241.
- [60] Skylark Wireless LLC. Accessed: Feb. 11, 2023. [Online]. Available: http://www.skylarkwireless.com/
- [61] R. Doost-Mohammady et al., "RENEW: Programmable and observable massive MIMO networks," in *Proc. 52nd Asilomar Conf. Signals, Syst.*, Comput., 2018, pp. 1654–1658.
- [62] E. Everett, A. Sahai, and A. Sabharwal, "Passive self-interference suppression for full-duplex infrastructure nodes," *IEEE Trans. Wireless Commun.*, vol. 13, no. 2, pp. 680–694, Feb. 2014.



Zhican Chen (Student Member, IEEE) received the B.S. degree from the University of Science and Technology of China, Hefei, China, in 2018, and the M.S. degree in electrical and computer engineering in 2020, from Rice University, Houston, TX, USA, where he is currently working toward the Ph.D. degree with Rice University under the supervision of Dr. A. Sabharwal. His research interests include wireless communications and wireless system design.



C. Nicolas Barati (Member, IEEE) received the Engineering Diploma in computer, telecommunications, and network engineering from the University of Thessaly, Volos, Greece, in 2011, and the Ph.D. degree in electrical engineering from the New York University Tandon School of Engineering, Brooklyn, NY, USA, in 2018. He is currently a Postdoctoral Research Associate with Rice University, Houston, TX. His research interests include wireless communications, massive MIMO, mmWave, and wireless security.



Jon Veihl (Member, IEEE) received the B.S. degree in electrical engineering from Michigan State University, East Lansing, MI, USA, in 1991, and the M.S and Ph.D. degrees in electrical engineering from the University of Illinois, Urbana-Champaign, IL, USA, in 1993 and 1996, respectively. He joined Raytheon Technologies, McKinney, TX, in 1996, where he worked on phased array antenna design for military and commercial systems. In 2000, he joined Comm-Scope and is currently a Senior Principal Antenna Engineer specializing in the design of passive and

active base station antennas for outdoor and indoor cellular systems. He holds more than 20 patents related to antenna design.



Clayton Shepard (Member, IEEE) received the B.S., M.S., and Ph.D. degrees in electrical engineering from Rice University, Houston, TX, USA, in 2008, 2012, and 2018, respectively. He is an Expert in scalable MIMO wireless systems. He founded the Argos project that prototyped the first Massive MIMO platform in 2012, and continues to be actively involved in its current evolution, the RENEW Project with Rice University (renew-wireless.org). He is the Founder and CTO of Skylark Wireless, which develops next-generation Massive MIMO solutions to

bridge the digital divide – connecting underserved rural communities to affordable broadband internet, and has provided the core R&D systems for multiple NSF Platforms for Advanced Wireless Research (PAWR) deployments. He was a Visiting Researcher with Motorola Research, Bell Labs, and Microsoft Research, and is the author of multiple foundational papers and patents on Massive MIMO. He was the recipient of the ACM Test-of-Time Award in 2022.



Ashutosh Sabharwal (Fellow, IEEE) received the B.Tech. degree from the Indian Institute of Technology Delhi, New Delhi, India, in 1993, and the M.S. and Ph.D. degrees from The Ohio State University, Columbus, OH, USA, in 1995 and 1999, respectively. He is currently the Department Chair and an Ernest D. Butcher Professor with the Department of Electrical and Computer Engineering, Rice University, Houston, TX, USA. His research interests include wireless theory, design, and large-scale deployed testbeds. He was one of the inventors of in-band full-duplex com-

munications, a technology used in both wireline and wireless systems. He is the Founder of the WARP Project (warp.rice.edu), an open-source project which is currently in use at more than 125 research groups worldwide and has been used by more than 500 research articles. He is currently leading several NSF-funded center-scale projects, notably Rice RENEW (renew-wireless.org), to develop an open-source software-defined wireless network platform. He was the recipient of the 2017 IEEE Jack Neubauer Memorial Award, the 2018 IEEE Advances in Communications Award, the 2019 ACM MobiCom Community Contribution Award, and the 2019 and 2021 ACM Test-of-time Awards. He is a Fellow of the National Academy of Inventors and the ACM (Association of Computing Machinery).